Effects of SiC content on the mechanical and thermophysical properties of 3D C$_f$/SiC–Al composites

Jia, Jinhao; Li, Cong; Chen, Qiang; Bai, Shuxin; Chang, Jin; Xiong, Degan; Gao, Mingqi; Li, Shun; Xiao, Jin

Important note
To cite this publication, please use the final published version (if applicable).
Please check the document version above.

Effects of SiC content on the mechanical and thermophysical properties of 3D Cf/SiC–Al composites

Jinhao Jia [a], Cong Li [b], Qiang Chen [a], Shuxin Bai [a,*], Jin Chang [c], Degan Xiong [a], Mingqi Gao [a], Shun Li [a,**], Jin Xiao [a]

[a] *College of Aerospace Science and Engineering, National University of Defense Technology, Changsha, 410073, China*
[b] *School of Materials Science and Engineering, Hubei University of Automotive Technology, Shiyan 442002, Hubei, China*
[c] *Kavli Institute of Nanoscience, Department of Quantum Nanoscience, Delft University of Technology, 2628CJ, Delft, the Netherlands*

ARTICLE INFO

ABSTRACT

3D Cf/SiC–Al composites were achieved through the pressure infiltration of liquid Al–Si alloy into porous 3D Cf/SiC preform, which was produced by different cycles of precursor infiltration and pyrolysis. The effect of silicon carbide volume fraction on the microstructure, anisotropic mechanical response, and thermophysical characteristics of the 3D Cf/SiC–Al composites was investigated. The results demonstrated that the initial microstructure of 3D Cf/SiC can be retained, and the obtained Cf/SiC–Al composites presented remarkable anisotropy characteristics. As the silicon carbide ceramics content increased from 12.5 vol% to 41.8 vol%, the thermal conductivity and thermal expansion coefficient of 3D Cf/SiC–Al composites decreased, whereas the bending strength initially increased and then decreased in the Z-direction. The bending strength perpendicular (Z) to the carbon cloth layer of 3D Cf/SiC–Al composites was higher than that of parallel (X–Y) to the carbon cloth layer. However, a significant anisotropy in the thermal conductivity values was the opposite. The 3D Cf/SiC–Al composite with 1ow ceramic content (17 vol%) had a higher thermal conductivity in the X–Y direction (64 W m^{-1} K^{-1}) than in the Z-direction (34 W m^{-1} K^{-1}). The thermal expansion coefficient of all the 3D Cf/SiC–Al composites along the X–Y direction also decreased initially and then increased in the range of 100–450 °C, which presents low expansion characteristics.

1. Introduction

Cf/SiC–Al composites, which are emerging potential composite materials for multifunctional application, have been proven to possess excellent mechanical properties [1–5]. Based on the practical service environment, different material designs are required on the Cf/SiC–Al composites. For high-temperature structure-supporting scenario, the composites should possess low expansion characteristics and high mechanical strength vertical to the load areas. As a high-temperature functional component, Cf/SiC–Al composites not only need good mechanical performance, but also retain a prominent thermal shock resistance [6–8]. Therefore, it is of considerable significance to evaluate the mechanical property and thermophysical properties performance of Cf/SiC–Al and further reveal its mechanism. In previous work, Chen et al. [9] successfully prepared Cf/SiC–Al composites, where the volume fraction of the fiber was 40%. they analyzed the compressive strength of

3D Cf/SiC–Al and revealed the mechanism of compression damage. Li et al. [10] studied the tensile behaviour and failure mechanism of Cf/SiC–Al composites and summarized the influence of fibre arrangement on the mechanical properties and fracture mode. Sun et al. [11] improved the ablation performance of the C/C–ZrC–SiC composite by introducing Al alloy, meanwhile, it showed that liquid Al can develop a dense oxide scale on the C/C–ZrC–SiC composite surfaces which contribute to obtaining a better anti-ablation property to protect the matrix. Our previous studies revealed that Cf/SiC–Al composites have excellent ablation resistance ability and mechanical properties [4,12]. But there is a long way to go to further promote the research and development of Cf/SiC–Al composites. To be more specific, the thermal stress factor (*TRS*) can be a good indicator of the high-temperature applications: TRS $= \sigma_b \lambda /_{E\alpha}$. where α is the Thermal expansion coefficient, σ_b is the bending strength,λis the thermal conductivity and E is the

---

* Corresponding author.
** Corresponding author.
E-mail addresses: shuxinbai@foxmail.com (S. Bai), linudt@163.com (S. Li).

Elastic Modulus. The larger the *TSR* value, the better the thermal shock resistance of the material. So the desirable C$_f$/SiC–Al composites should have an excellent thermal conductance vertical to the contact areas, and a low thermal expansion parallel to the function surface. The *TRS* demonstrate that the high-temperature applications of C$_f$/SiC–Al composites is closely related to their strength and thermophysical properties [13–23]. Up to now, for C$_f$/SiC infiltrated with Al alloy, the research on mechanical properties was only focused on the unidirectional compression strength, while the anisotropy bending strength and thermophysical property of such composites have not been revealed so far. Therefore, this paper is designed to study and understand the effects of SiC volume fraction on the microstructure, anisotropic mechanical properties, and thermophysical characteristics of C$_f$/SiC–Al.

In our works, 3D C$_f$/SiC–Al composites were fabricated by a combined process of precursor infiltration and pyrolysis (PIP) and vacuum pressure infiltration (VPI). The effect of silicon carbide volume fraction on the microstructures, anisotropy mechanical property, and thermophysical properties of 3D C$_f$/SiC–Al composites were thoroughly analyzed.

2. Experimental

3D needled C$_f$ preform with a volume fraction of 26% was used as a skeleton. Polycarbosilane (PCS) was dissolved in xylene and used acted as the precursor. The porous 3D C$_f$/SiC composites were obtained by PIP which was repeated for different times. The obtained C$_f$/SiC composites had different open porosity and SiC content. The C$_f$/SiC composites with SiC volume fractions of 12.5, 16.6, 30.7 and 41.8 vol% were denoted as 'C$_f$/SiC13,' 'C$_f$/SiC17,' 'C$_f$/SiC31' and 'C$_f$/SiC42,' respectively. Alloy A356 was used as filler. Meanwhile, the composition of the metal matrix and details of the preparation process are available in our previous work [4]. The fabrication procedure of 3D C$_f$/SiC composites and the infiltration of Al alloy for obtaining 3D C$_f$/SiC–Al composites is shown in Fig. 1. The obtained 3D C$_f$/SiC–Al composites and their corresponding reinforcement volume fraction are summarized in Table 1, in which the 3D C$_f$/SiC–Al composites with SiC volume fractions of 12.5, 16.6, 30.7, and 41.8 vol% were denoted as 'C$_f$/SiC13–Al,' 'C$_f$/SiC17–Al,'

Table 1
Reinforcement content, porosity, density and thermal diffusivity of C$_f$/SiC–Al composites.

Composites	SiC (vol %)	C$_f$ (vol %)	Density (g/cm^3)	Porosity (%)	Thermal diffusivity - XY (mm^2/s)	Thermal diffusivity - Z (mm^2/s)
C$_f$SiC13-Al	12.5	26.2	2.43	3.2	30.928 ± 6	15.815 ± 6
C$_f$SiC17-Al	16.6	26.2	2.37	5.2	28.375 ± 3	13.462 ± 5
C$_f$SiC31-Al	30.7	26.2	2.32	10	15.909 ± 4	5.450 ± 5
C$_f$SiC42-Al	41.8	26.2	2.30	12	8.208 ± 2	3.936 ± 4

'C$_f$/SiC31–Al' and 'C$_f$/SiC42–Al,' respectively.

The size of samples obtained after Al infiltration was 72 mm × 36 mm × 10 mm. The sample sizes and equipment used for morphology and phase were described in detail in our previous study [4,12]. Pore distribution was obtained by Mercury porosimeter(IV 9500, Micromeritics Instrument Corporation). The CTE of C$_f$/SiC–Al composites (sample size: 5 mm × 5 mm × 25 mm) were analyzed using a dilatometer (DIL 402 EP, Netzsch Corporation, Germany). Meanwhile, the CTE of C$_f$/SiC–Al composites was examined with a heating rate of 5 °C/min. The TC values of samples (Φ12.6 mm × 4 mm) were obtained using a Netzsch LFA 427 laser flash apparatus. The thermal conductivity of the C/SiC composites was calculated using the following equations:

$$\lambda = \alpha \times \rho \times C_p \tag{1}$$

where λ is the thermal conductivity, a is the thermal diffusion, ρ is the density, C$_p$ is the specific heat.

The three-point-bending method was used to quantify the mechanical properties of the composites. The span was 30 mm, samples sizes were 40 × 4 × 3 mm, and the headpressing rate was 0.5 mm min^{-1}.

3. Test results and discussions

3.1. Microstructure of the C$_f$/SiC–Al composites

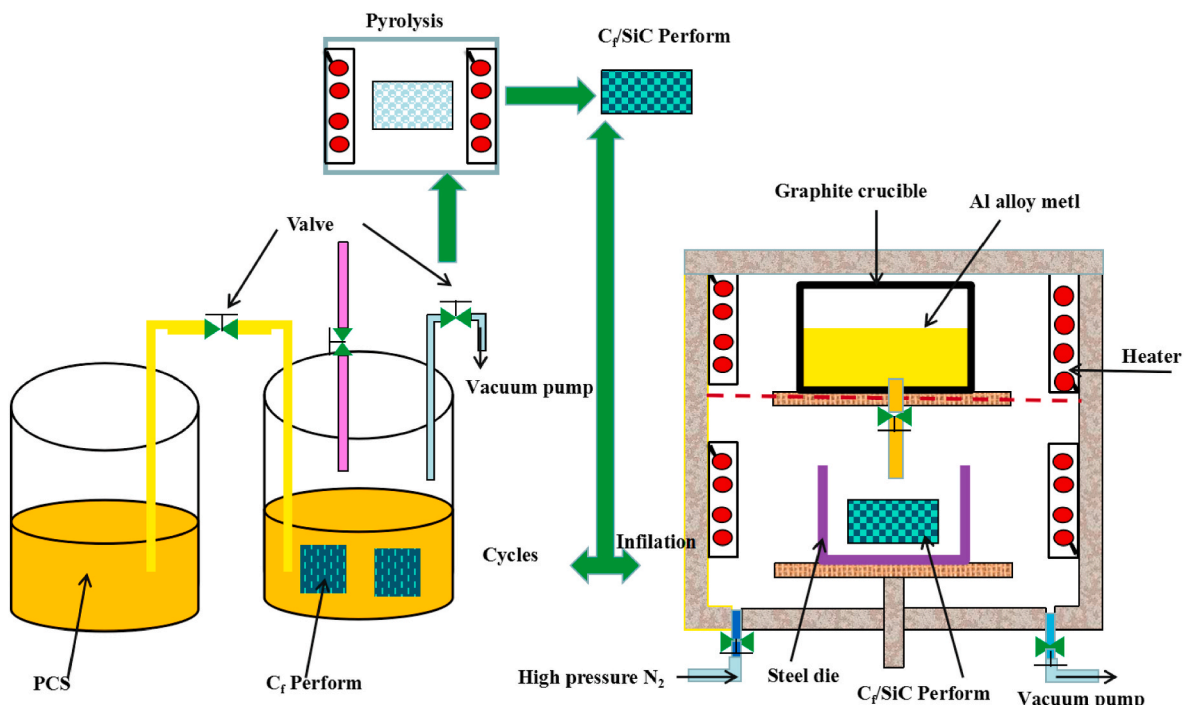The size distributions for Cf/SiC13, Cf/SiC17, Cf/SiC31, and Cf/

Fig. 1. Schematic diagram of the preparation process of C$_f$/SiC–Al composites.

SiC42 are shown in Fig. 2. It shows that the general trends were similar in all cases. However, differences can also be noticed. For example, $C_f/$ SiC13 and $C_f/$SiC17 show uni-modal distribution with peaks. As shown in Fig. 2a, the size of full-open pores ranges from 50 nm to 100,000 nm. Though the pore size distributions of $C_f/$SiC13 and $C_f/$SiC17 were slightly different, the relatively large pores are distributed at about 50,000 nm in general. The distribution becomes narrow and close to the single-sized pores as SiC content increases. In Fig. 2b, the pore size distributions have additional peaks of $C_f/$SiC31 and $C_f/$SiC42 in the relatively small pore (>600 nm) region. The size distribution of the fully open pores (Fig. 2b) reveals that nanoscale open pores or channels exist in the $C_f/$SiC composites and can be filled with Al alloy. The precursor of the ceramic was PCS, which inclined to conglutinate adjoining the fibre bundles; thus, inter-bundle channels tend to become smaller with the increase in SiC content, which results in lessening pores. By contrast, the median pore diameter tended to decrease as the amount of SiC content increased, which indicates that adding the number of PIP cycles will reduce pores with relatively large sizes. The test results show that the overall through–hole ratios of $C_f/$SiC13, $C_f/$SiC17, $C_f/$SiC31 and $C_f/$SiC42 were 55.0568%, 51.8824%, 31.8614%, and 20.2070%, respectively.

The microstructure images of the four kinds of 3D $C_f/$SiC–Al composites are shown in Fig. 3a–d. Fig. 4 is the XRD patterns of the obtained 3D $C_f/$SiC–Al composites. The 3D $C_f/$SiC–Al composites are composed of SiC, Si, Fe, and Al. The off-white and dark grey areas in Fig. 3 are Al–Si alloy and $C_f/$SiC, respectively. Notable differences were found in the microstructures of the composites at low magnification. As shown in Fig. 3 a–d, the grey-black areas ($C_f/$SiC) gradually increase, the dark grey zone is surrounded by off-white areas (Al alloy), and no defects can be found. Carbon cloth layers and needled fibers are clearly visible. By contrast, Fig. 3 c, d, j, and k show a noncontinuous, island-like Al–Si alloy. Almost no evident defects in the matrix and inter-bundle were observed because of the infiltration of the Al–Si alloy. However, the high-magnification images of $C_f/$SiC41–Al (Fig. 3 e-h) reveal that SiC content leads to the observed the morphology of the 3D $C_f/$SiC–Al composites. Silicon carbide ceramics matrix mainly fills the intra-bundles pores and silicon carbide ceramics matrix surrounding the fiber bundles can comprise a protection layer to prevent it from corrosion by Al alloy melt. The C_f are bonded together by the SiC derived from PIP. The initial microstructure of 3D $C_f/$SiC was retained, and the obtained 3D $C_f/$SiC–Al composites presented a remarkable anisotropy structure. Meanwhile, a small number of pores remained in the fibre bundle (Fig. 3 f). The intra-bundle pores in $C_f/$SiC41–Al has a diameter of 20–50 μm. The intra-bundle defects are usually formed in the adjacent space of fibres. The much larger capillary resistance force makes the pores difficult to completely fill with the Al–Si alloy or PCS in the infiltration process. Fig. 3 g shows that inter-bundle channels have relatively large holes and can be easily infiltrated by the Al–Si alloy in

auxiliary pressure because of the absence of a C_f skeleton. This can be attributed to the preparation method, which overcame capillary force in preforms to a certain extent. Based on the analysis, Al–Si alloy can effectively infiltrate the large inter-bundle channels but hardly fill the intra-bundle interspace, which has a much larger capillary force [28, 29]. The porosity and density of the obtained 3D $C_f/$SiC–Al are listed in Table 1. It shows that the 3D $C_f/$SiC–Al composites had lower density and higher porosity as SiC content increased. The 3D $C_f/$SiC13–Al had the highest density and the lowest porosity. This result indicates that infiltration Al results of the porous 3D $C_f/$SiC13 preform are promising, and the majority of pores were completely filled. However, the porosity of $C_f/$SiC42–Al reaches 12%. It means increasing PIP cycle fills the inter-bundle pores of the porous C_f skeleton, resulting in the formation of a large number of closed voids.

3.2. Mechanical properties

Anisotropy is an important feature that influences the service condition. One of the main aims of this part study is to investigate the mechanical characteristic of 3D $C_f/$SiC–Al composites. The needle-punched C_f body consisted of carbon cloth layer, short-cut fabric, and needling fibres. Thus, the orientation and content of fibres are different in 3D space, and 3D $C_f/$SiC–Al composites present mechanical anisotropy. The quantitative mechanical characteristic of the 3D $C_f/$SiC–Al composites were compared with the corresponding 3D $C_f/$SiC composites used as reinforcement as shown in Fig. 5 b. The flexure strength values perpendicular to the carbon woven fibre cloths of 3D $C_f/$SiC13–Al, $C_f/$SiC16–Al, $C_f/$SiC31–Al and $C_f/$SiC42–Al were 249, 343, 454, and 423 MPa, respectively, which were 404.8%, 516.7%, 204.6% and 29.7% higher than those of the corresponding 3D $C_f/$SiC preform. These results indicate that the filled alloy had substantially enhanced the mechanical characteristic of the 3D $C_f/$SiC composites. Meanwhile, silicon carbide is the main bearing phase and the aluminum matrix mainly plays the role of transmitting the load. The enhancement in the flexure strength of the 3D $C_f/$SiC–Al composites are attributed to two reasons. First, the majority of open pores were filled with Al–Si alloy, which ensures the effective load transfer between the Al–Si matrix and reinforcement and improves the reinforcement that bears the load. Also the more silicon carbide content, the stronger the load-bearing capacity. Second, the composites became dense; therefore, the primary pore cannot act as a source of cracks. This change resulted in the reduction of crack propagation in all directions. Fig. 5 c shows the flexure strength versus strain curves of the 3D $C_f/$SiC–Al composites loaded perpendicular (Z) or parallel (X–Y) to the carbon cloth layer. The flexure strength of Z-direction was higher than that along the X–Y direction. Zhaofeng Chen et al. found that the fracture of 3D $C_f/$SiC–Al was likely to induce at the inter-bundle pores and then extend straight along with the carbon cloth layer. Thus, when loading is performed parallel to the carbon cloth
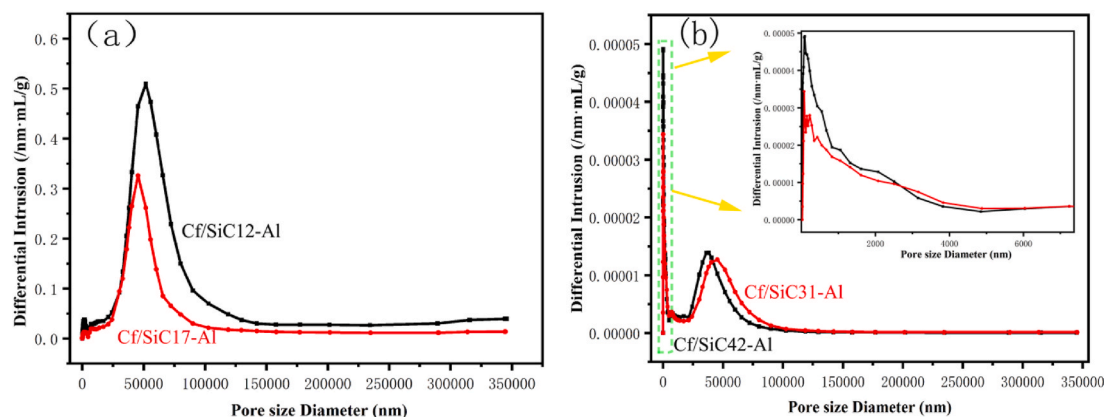

Fig. 2. (a) Pore-size distributions of the 3D $C_f/$SiC13 and $C_f/$SiC17 preforms; (b) Pore-size distributions of the $C_f/$SiC31 and $C_f/$SiC42 preforms.
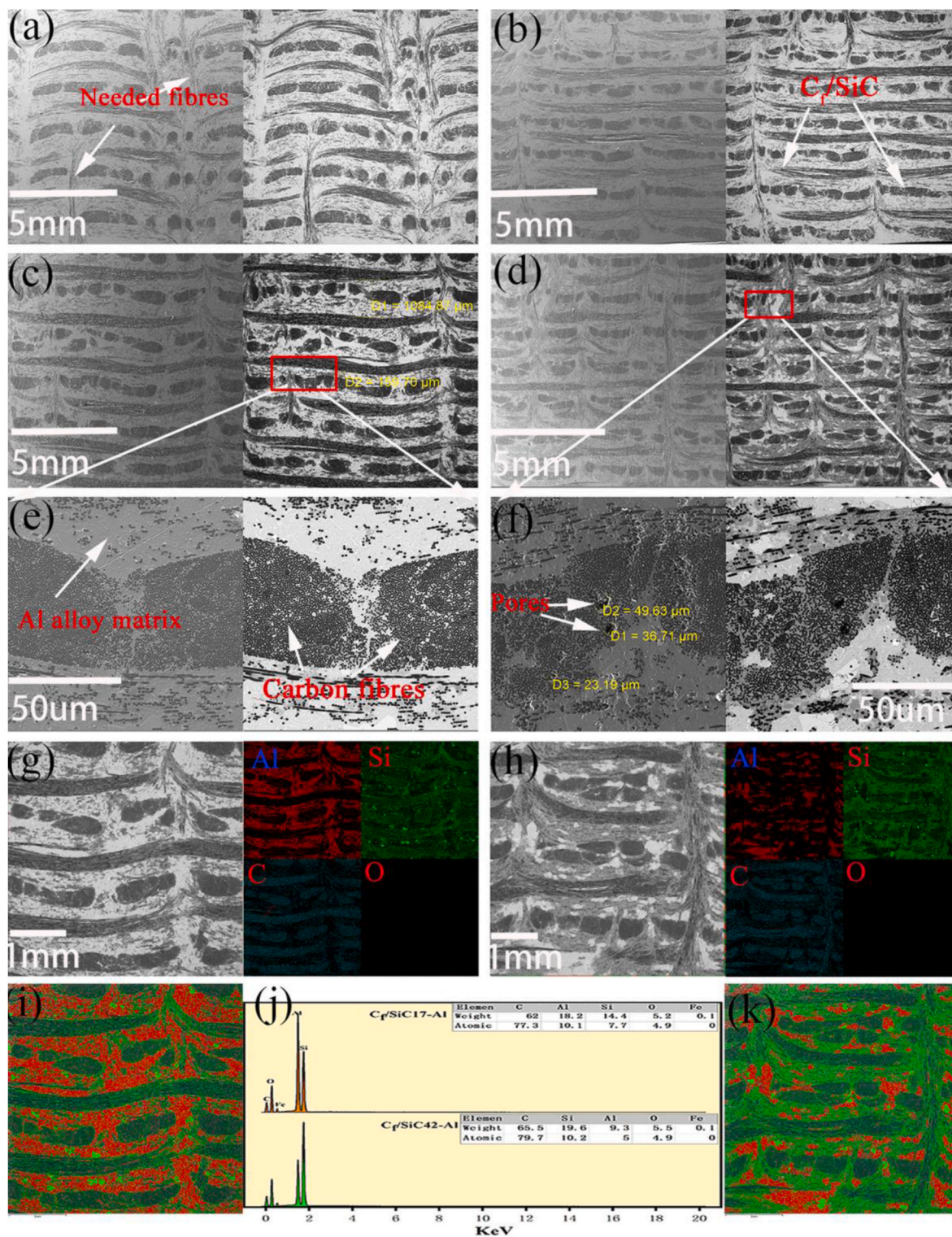
Fig. 3. SEM micrographs of the as-processed composites; (a,b) the microscopic morphology of the C$_f$/SiC13–Al and C$_f$/SiC17–Al; (c, d) the microscopic morphology of the C$_f$/SiC31–Al and C$_f$/SiC42–Al; (e, f) the enlarged view of the area in Fig. 3 (b) and (c); (g,i) EDS mapping analysis images of the C$_f$/SiC17–Al composite; (h, k) EDS mapping analysis images of the C$_f$/SiC17–Al composite; (j) The result of EDS mapping analysis of Fig. 3 (g) and (h).

layer, cracks could spread along with the inter-layer pores and propagate vertically to shear the fibres. However, the longitudinal direction of the warp is parallel to the loading direction, which cannot withstand stress and naturally propagates cracks. When the carbon cloth layer was perpendicular to the loading direction, the Al alloy and silicon carbide ceramics can act as effective energy dissipators to hold back crack propagation and reduce secondary cracks. The majority of the fibres,

arranged perpendicular to the load direction, obtained a good strengthening effect and mechanical response. Therefore, a remarkable anisotropy in bending strength was observed, that is, loading perpendicular to the carbon cloth showed a higher strength compared with loading parallel to the carbon cloth layer.

The bending strengths perpendicular and parallel to the woven fibre increased initially together with the SiC content. A similar trend was also
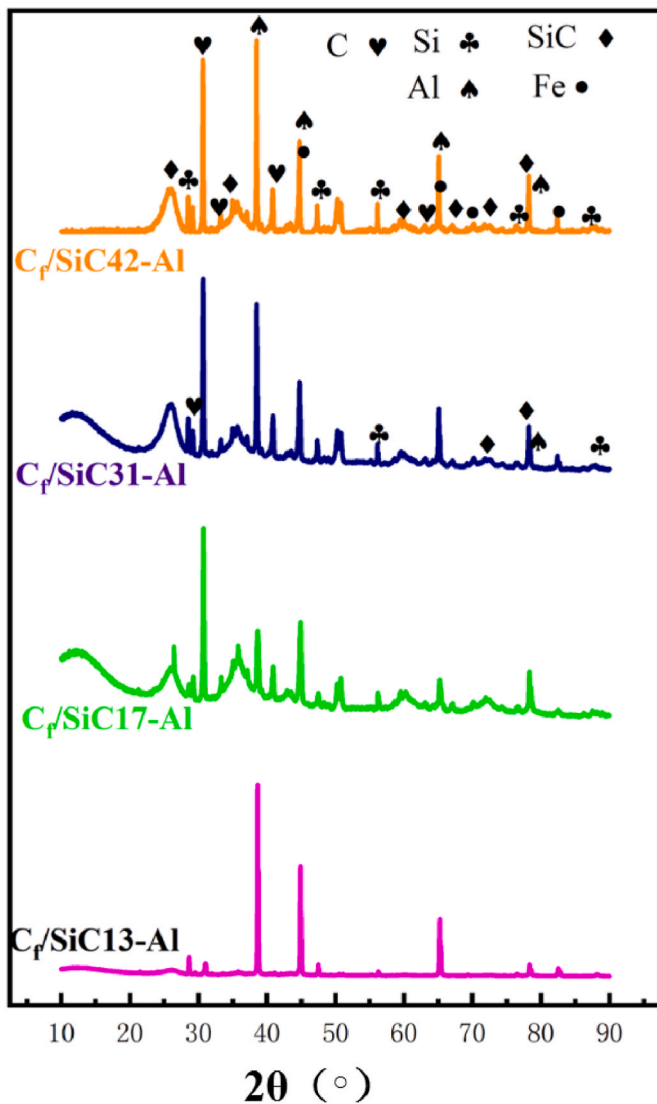
Fig. 4. XRD patterns of the C_f/SiC–Al composites.

found in the 3D C_f/SiC composites whtion was perpendicular to the woven fibre. Thus, the bending strength of the composites was associated with the SiC content, which played an essential role in bearing and transfer loading. However, the bending strength of the 3D C_f/SiC–Al composites increased initially and then decreased in the direction perpendicular to the carbon cloth layers as the SiC content increased from 13 vol% to 42 vol%. The decreased bending strength values can be attributed to the inter-bundle and inter-layer pores in the composites. Bending strength is susceptible to closed pores; the porosity of 3D C_f/SiC42–Al reached 12%; As a result, 3D C_f/SiC42–Al shows a lower bending strength than 3D C_f/SiC31–Al in the direction perpendicular to the carbon cloth layers. As shown in Fig. 5 c-e, the typical bending stress–displacement curves of 3D C_f/SiC42–Al and 3D C_f/SiC31–Al composites in the direction perpendicular to the carbon cloth layers are very close. Stress increased monotonously with displacement until the stress reached the highest point, the curve of 3D C_f/SiC42–Al declined precipitously, which can be inferred that the composite presents a typical brittle rupture. The fracture surfaces of 3D C_f/SiC13–Al, C_f/SiC17–Al and C_f/SiC31–Al under bending failure are jagged and stepped, and the majority of long bundles are pulled out (Fig. 6 a–c). In comparison, the fracture surface of C_f/SiC42–Al is relatively flat and flush with less pronounced and shorter pull-out. Cf/SiC13–Al exhibits a more crooked non-linear bending stress–strain curve to the ultimate

brittleness failure, and few obvious initial linear domain was identified at low loads, which was different from that of C_f/SiC42–Al. A large number of fibre bundles were tensile ruptured and obviously pulled out (Fig. 6 d). The Cf–SiC interfaces and SiC–Al is mechanical interlocking, the non-linear behaviour of C_f/SiC13–Al composites can be attributed to recombination debonding at interfaces [24,25].

3.3. Thermophysical properties of C_f/SiC–Al composites

Fig. 7 shows the CTE curves of the 3D C_f/SiC–Al composites as a function of temperature. The average CTE values of 3D Cf/SiC13–Al, C_f/SiC17–Al, and C_f/SiC31–Al were in the range of 2.0–4.3×10^{-6} K^{-1} from 100 °C to 450 °C. Importantly, the CTE values of 3D C_f/SiC42–Al and C_f/SiC31–Al decreased considerably with the increase of SiC content. The average CTE value along the carbon cloth layer was less than 2.5×10^{-6} K^{-1} from 100 °C to 450 °C. Moreover, the CTE values of 3D Cf/SiC13–Al and C_f/SiC17–Al composites versus temperature initially decreases and then rises slightly. However, the curves of the CTE values of C_f/SiC31–Al and C_f/SiC41–Al present an inconspicuous fluctuation along the direction of the fibre cloth from 100 to 450 °C. Three major factors affect the fluctuations in the CTE values of the 3D C_f/SiC–Al composites. First is the intrinsic thermal expansion properties of C_f reinforcement. The CTE of C_f along the axis is -0.7×10^{-6} K^{-1}, which is suppressed the thermal expansion of SiC and Al [26,29]. SiC is wrapped on the outer layer of C_f, and the negative axial expansion of C_f is limited. However, the material still exhibits a considerably low expansion when tested at a lower temperature because of the high C_f content. Second is that residual pores and microcracks form in the composites after preparation. The thermal expansion of C_f/SiC–Al composites could reduce the porosity and heal cracks, which offsets the expansion of the matrix and reinforcement. Defects provide space for the expansion of the matrix; hence, filling the defects will decrease or maintain the CTE. This phenomenon explains the inconspicuous fluctuation in the CTE curves of C_f/SiC31–Al and C_f/SiC41–Al. When the temperature is increased to a certain value, the majority of pores and gaps are filled. Subsequently, the thermal expansion performance will be affected by the expansion of SiC and Al, and the CTE will gradually increase. Therefore, the CTE values of the 3D C_f/SiC–Al composites initially dropped and then increased. Most importantly, the CTE of the 3D C_f/SiC–Al composites were substantially influenced by internal stress. The CTE of the composites was calculated based on the Eshelby model [27,28]:

$$\alpha_c = \frac{\Delta L}{L_0 \bullet \Delta T} = \frac{\sigma_0 + \sigma_{\Delta T}}{C_m (S - I) \bullet \Delta T} + \alpha_m \tag{2}$$

where α is the CTE; L_0 is the initial length of the specimen; ΔL is the length dimension variation; σ_0 is the residual stress of the matrix at room temperature; $\sigma_{\Delta T}$ is the average residual compressive stress at high temperature; C_m and S are the matrix stiffness tensor and Eshelby tensor, respectively; and I is the unit matrix. Subscripts c, m, and ΔT refer to composite, substrate and temperature variation, respectively. The C_f/SiC–Al composites were prepared by VPI method. During the cooling process, the CTE difference between C_f/SiC and the Al–Si alloy led to a large thermal residual stress in the matrix. When the test temperature rises, the local tensile stress is relieved, which means that the value of σ_0 in Eq. (2) becomes lower. Meanwhile, the high-temperature test process can increase the residual compressive stress and therefore reduce the CTE. The CTE value of C_f along axis a was -0.7×10^{-6} K^{-1}, which suppressed the thermal expansion of SiC. The CTE of SiC is 4.6×10^{-6} K^{-1} [26,30], which also restrains Al alloy. The higher the silicon carbide content, the stronger the ability to inhibit the expansion of the aluminum alloy, so the lower the thermal expansion coefficient of composites. These factors led to the formation of a large amount of compressive stress inside the material. According to Eq. (2), the compressive stress increases with the increase in content, which results in the decrease of CTE.
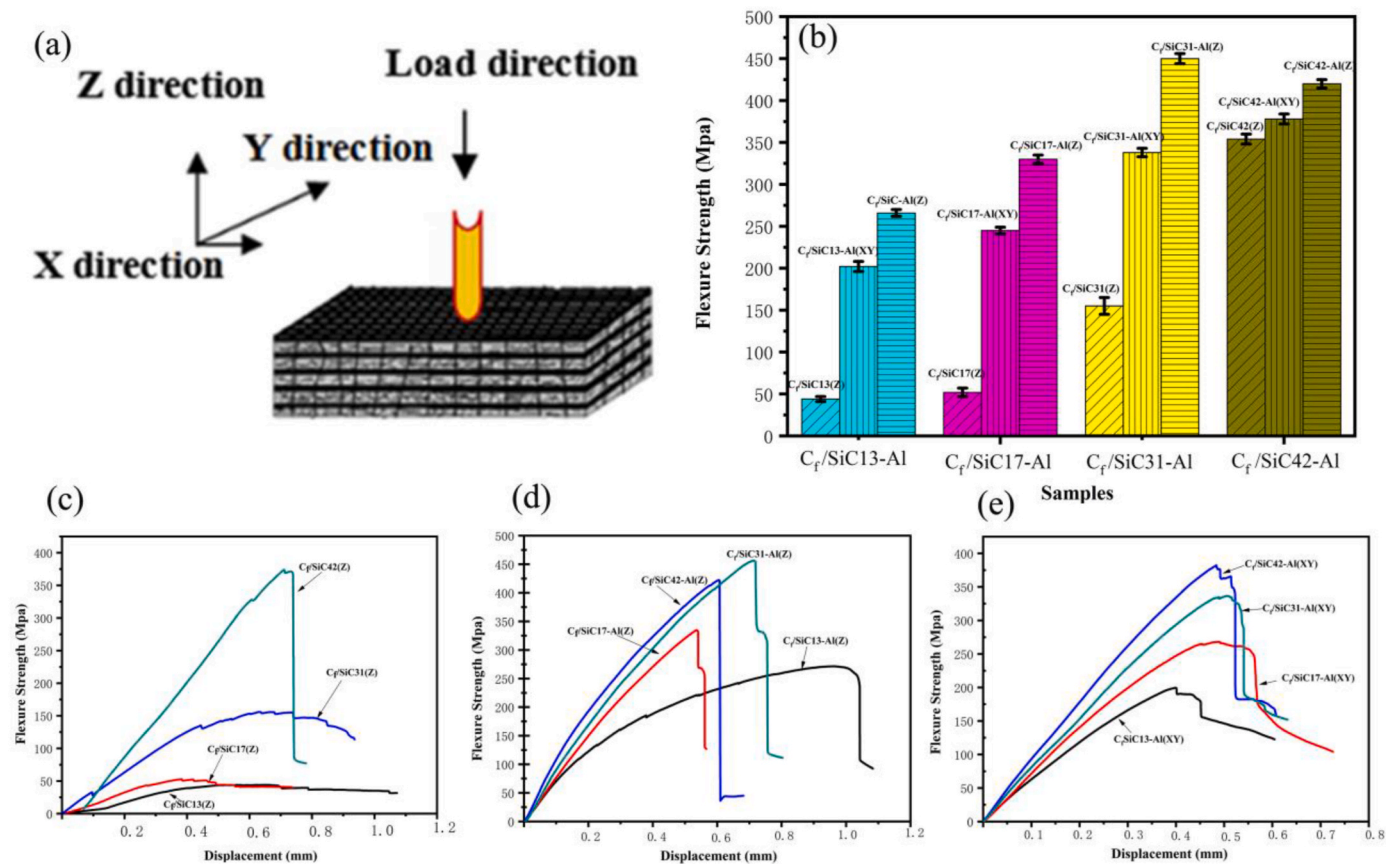
Fig. 5. (a) Schematic diagram of load test direction; (b) Comparison of mechanical properties of C_f/SiC preforms and C_f/SiC–Al composites; (c) Typical stress-displacement curves of the C_f/SiC preforms; (d) Typical stress-displacement curves of the C_f/SiC–Al (Z) composites; (e) Typical stress-displacement curves of the C_f/SiC–Al (XY) composites.
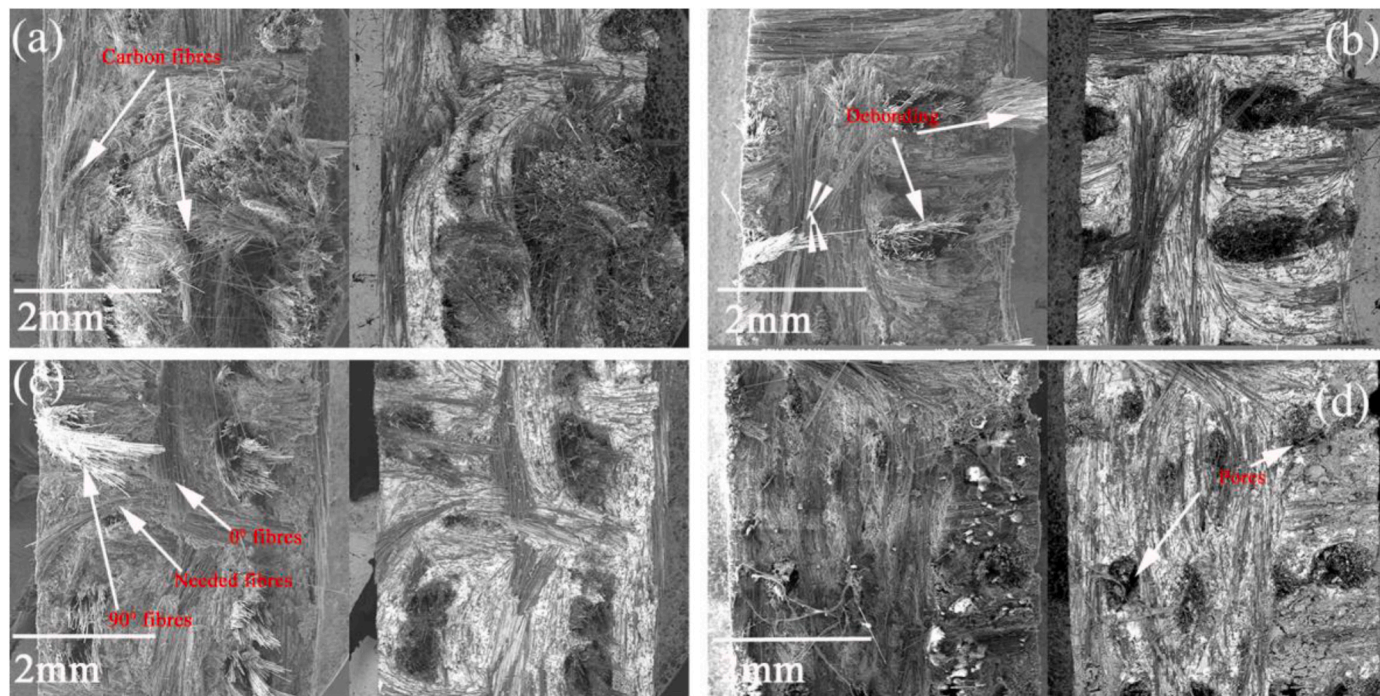

Fig. 6. The fracture morphologies of (a) C_f/SiC13–Al composites, (b) C_f/SiC17–Al, (c) C_f/SiC31–Al and (d) C_f/SiC42–Al composites.
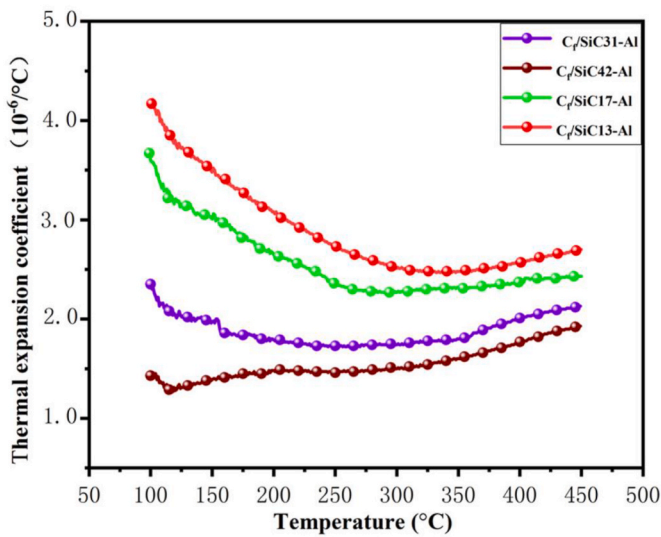
Fig. 7. CTE curves of C$_f$/SiC–Al composites.

Thermal conductivity (TC) is strongly influenced by the arrangement of the reinforcement, the relative volume fraction (*V*), and the intrinsic TC of each phase. Fig. 8 shows that the TCs of the C$_f$/SiC–Al composites drops in both directions with the increase of SiC content. C$_f$/SiC13–Al

has a higher average TC than the other composites. The difference was obvious when the volume fractions of SiC were 17% and 42%, in which the average TC$_{\parallel(carbon\ cloth\ layer)}$ was 64 and 34 W m^{-1} K^{-1}, respectively. The tested directions were perpendicular (Z) and parallel (X–Y) to the carbon cloth layer (Fig. 8 b, c). The TC values of all the composite show remarkable anisotropy, that is, TC$_{\parallel(carbon\ cloth\ layer)}$ was higher than TC$_{\perp(carbon\ cloth\ layer)}$. This behaviour can be explained by using a network model to evaluate λ$_c$ as follows:

$$\lambda_c = f[\lambda_{Al}, \lambda_{SiC}, \lambda_{C_f}, V, G(f)] \tag{3}$$

where *G(f)* is the distribution function of reinforcement. Though the 3D C$_f$ skeleton had a fibre volume fraction of 26%, the volume fraction of the needled fibres was only about 1%. If the influence of the needle-punched C$_f$ (Fig. 8 b) is ignored, heat transfer perpendicular and parallel to the carbon cloth layer can be estimated by electrical network analogy as shown in Fig. 8 d.

The radial TC of the 3D C$_f$/SiC–Al composites at room-temperature TC$_{\perp(carbon\ cloth\ layer)}$ can be regarded as an in-series combination of the adjacent two structure units as shown in Fig. 8 d. For the TC$_{\perp(carbon\ cloth\ layer)}$, the needled channels filled with Al and silicon carbide ceramics are the main heat conduction mediums. However, the heat transfer of the carbon cloth layer perpendicular to the fibre axis plays a choking-off effect. The dominant heat transfer of C$_f$ is in the direction along the fibre axis. TC can be evaluated by assuming the in-parallel combinations. The conduction of thermal energy occurs through the flow of phonons along with the C$_f$ of the carbon cloth layer, which means that

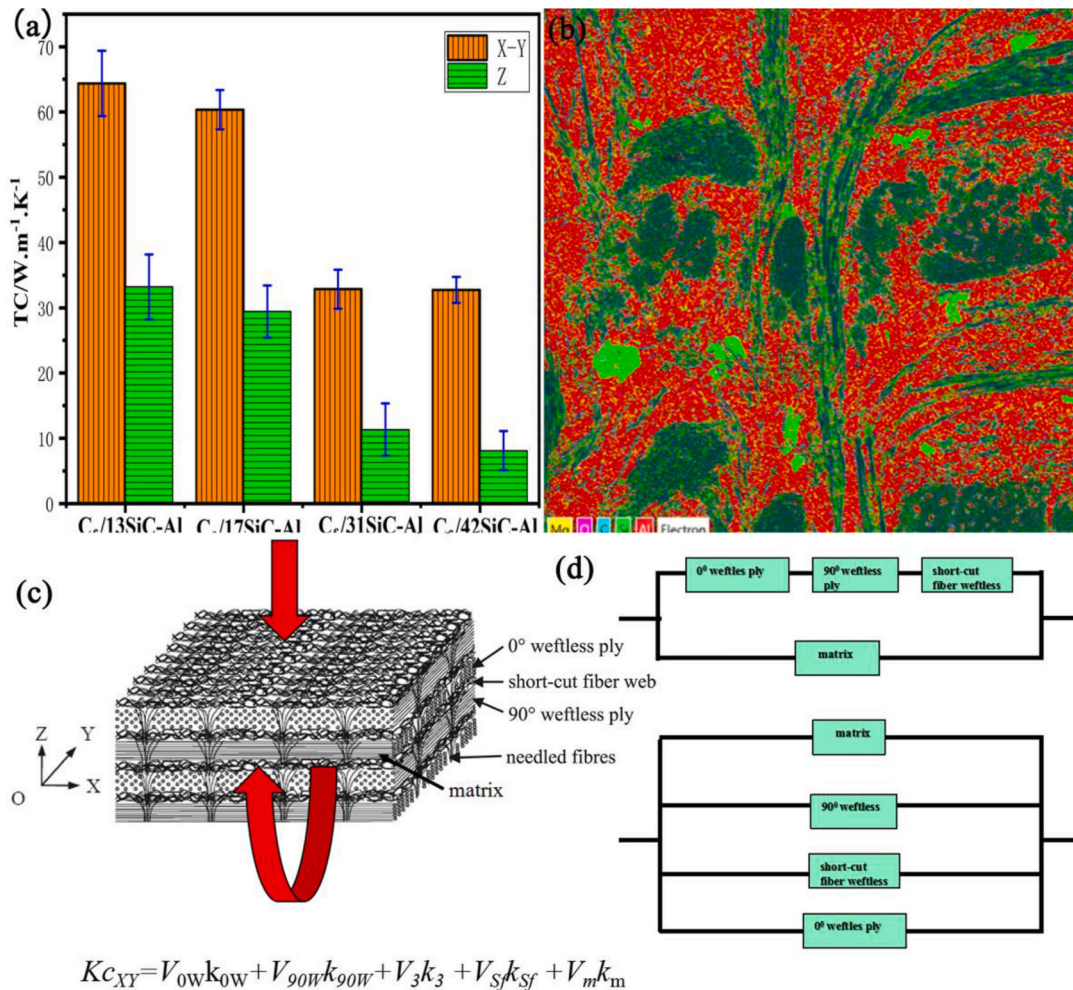$$Kc_{XY} = V_{0W}k_{0W} + V_{90W}k_{90W} + V_3k_3 + V_{Sf}k_{Sf} + V_mk_m$$

Fig. 8. (a) TC of C$_f$/SiC–Al composites; (b) Mapping of C$_f$/SiC–Al composites; (c) Schematic diagram of heat conduction direction; (d)The structural units for evaluating the radial and axial TCs of C$_f$/SiC–Al composite.

the heat transfer has multiple channels. Therefore, TC$_{\perp\text{(carbon cloth layer)}}$ was relatively lower than TC$_{\parallel\text{(carbon cloth layer)}}$ with the same SiC volume fraction. This result is opposite the prediction because SiC has a higher TC. An increase in SiC content means a decrease in Al matrix content, and the TC of SiC is higher than that of the Al alloy. Moreover, the C$_f$/SiC–Al composites with a higher volume fraction of SiC had a lesser contact area between Al–Si and SiC matrix, which led to a smaller scattering effect during heat flow and produce a higher TC. The results indicate that the TC of 3D C$_f$/SiC–Al composites are influenced by reinforcement arrangement and other factors. The considerably decreased TC can be attributed to the incremental heat resistance of defects. Table 1 summarises the porosities and thermal diffusion coefficients of the of 3D C$_f$/SiC–Al composites. Notably, TC was strongly affected by the defects. Porosity increased roughly from 3.3% to 12% as the SiC content increased from 12.6 vol% to 41.8 vol%. The porosities of the 3D C$_f$/SiC–Al composites show a monotonically increasing trend. The repeating transformation of PCS into SiC during the PIP process, accompanied by volume contraction, will unavoidably form closed pores. Moreover, the number of closed pores will escalate with the increase in PIP cycles. Therefore, the C$_f$/SiC composite inevitably contained more small closed pores as the SiC content increased. A large number of closed pores cannot be filled by Al alloy. The existence of pores in the composites greatly increases the heat obstacle between electronic and phononic heat conductions. The heat conduction in these closed pores mainly relies on the low heat radiation and gas molecular vibration. Therefore, the TC of 3D C$_f$/SiC–Al decreased with the increase in silicon carbide ceramics volume fraction in both directions.

4. Conclusions

The current work reports the effect of SiC content on the mechanical and thermophysical properties of 3D C$_f$/SiC–Al composites fabricated by PIP and VPI processes. Bending strength increased in the X–Y direction but increased initially and then decreased in the Z-direction as the SiC content increased from 12.5 vol% to 41.8 vol%. In all four composites, C$_f$/SiC31–Al had the maximum bending strength of 454 MPa along the Z-direction, which was two times that of C$_f$/SiC. The porosity gradually increased roughly from 3.3% to 12% with the increase of SiC content from 12.6 vol% to 41.8 vol%, which resulted in the decrease in TC with the increase in SiC content in both directions. In addition, the C$_f$/SiC–Al composites had decreased CTEs according to the stress-induced strain mechanism because of the low expansion properties of the reinforcement and the large thermal residual stress in the matrix.

Declaration of competing interest

The authors declare that they have no known competing financial interests or personal relationships that could have appeared to influence the work reported in this paper.

References

[1] H. Mei, H.Q. Li, Q.L. Bai, Q. Zhang, L.F. Cheng, Increasing the strength and toughness of a carbon fiber/silicon carbide composite by heat treatment, Carbon 54 (2013) 42–47.
[2] H.Z. Wang, X.D. Li, J. Ma, G.Y. Li, T.J. Hu, Fabrication of multi-walled carbon nanotube-reinforced carbon fiber/silicon carbide composites by polymer infiltration and pyrolysis process, Compos. Sci. Technol. 72 (3) (2012) 461–466.
[3] Y.D. Xu, L.T. Zhang, L.F. Cheng, D.T. Yan, Microstructure and mechanical properties of three-dimensional carbon/silicon carbide composites fabricated by chemical vapor infiltration, Carbon 36 (7–8) (1998) 1051–1056.
[4] J. Jia, S. Bai, D. Xiong, et al., Microstructure and ablation behaviour of a C$_f$/SiC-Al composite prepared by infiltrating Al alloy into C$_f$/SiC, J. Alloys Compd. 895 (2021) 162430, 2021.
[5] Q. Zhang, G. Li, A review of the application of C/SiC composite in thermal protection system, Multidiscip. Model. Mater. Struct. 5 (2009) 199–203.
[6] Y. Li, L. Zhang, R. He, et al., Integrated thermal protection system based on C/SiC composite corrugated core sandwich plane structure, Aero. Sci. Technol. 91 (2019) 607–616.
[7] Srdo Pina, L.C. Pardini, I. Yoshida, Carbon fiber/ceramic matrix composites: processing, oxidation and mechanical properties, J. Mater. Sci. 42 (2007) 4245–4253.
[8] W. Krenkel, F. Berndt, C/C-SiC composites for space applications and advanced friction systems, Mater. Sci. Eng. 412 (2005) 177–181.
[9] J. Liao, Z. Chen, B. Li, et al., Microstructure and mechanical properties of C$_f$/SiC-Al composites fabricated by PIP and vacuum pressure infiltration processes, J. Alloys Compd. 803 (2019) 934–941.
[10] Liping Xue, Zhaofeng Chen, Jiahao Liao, et al., Compressive strength and damage mechanisms of 3D needle-punched C$_f$/SiC-Al composites, J. Alloys Compd. 853 (2021) 156934.
[11] Yabin Chang, Wei Sun, Xiong Xiang, et al., A novel design of Al-Cr alloy surface sealing for ablation resistant C/C-ZrC-SiC composite, J. Eur. Ceram. Soc. 37 (2017) 859–864.
[12] J. Jia, J. Xiao, D. Xiong, et al., Ablation properties of C$_f$/SiC$_p$-Al self-transpiration cooling composites, Mater. Lett. 285 (2020) 129022.
[13] H. Mei, L. Cheng, L. Zhang, X. Luan, P. Fang, J. Zhang, Thermal shock behavior of two-dimensional C/SiC composites in controlled atmospheres, J. Mater. Sci. 40 (16) (2005) 4261–4265.
[14] S. Kumar, A. Kumar, K. Sampath, V.V. Bhanu Prasad, J.C. Chaudhary, A.K. Gupta, Rohini G. Devi, Fabrication and erosion studies of C-SiC composite Jet Vanes in solid rocket motor exhaust, J. Eur. Ceram. Soc. 31 (2011) 2425–2431.
[15] M. Aparicio, A. Durán, C/SiC composites for high temperature structural applications. Part II: oxidation protection systems, Boletin de la Sociedad Espanola de Ceramicay Vidrio 40 (2001) 7–15.
[16] Y. Xu, et al., A multi-layer integrated thermal protection system with C/SiC composite and Ti alloy lattice sandwich, Compos. Struct. 230 (2019) 111507.
[17] W. Li, Z.H. Chen, Pore geometry of 3D-C$_f$/SiC composites by mercury intrusion porosimetry, Ceram. Int. 35 (2009) 747–753.
[18] L.F. Cheng, Y.D. Xu, L.T. Zhang, et al., Effect of glass sealing on the oxidation behavior of three dimensional C/Si C composites in air, Carbon 39 (2001) 1127–1133.
[19] Cheng Laifei, et al., Effect of carbon interlayer on oxidation behavior of C/SiC composites with a coating from room temperature to 1500°C, Mater. Sci. Eng. (2001).
[20] Y.A.N. Zhi-qiao, X.I.O.N.G. Xiang, X.I.A.O. Peng, Feng Chen, Hong-bo Zhang, Bai-yun Huang, Oxidation Behavior of Oxidation Protective Coatings for C/C-SiC Composites at 1500 °C, Trans. Nonferrous Met. Soc. China, 2009.
[21] Z.Q. Yan, X. Xiong, P. Xiao, et al., Si-Mo-SiO$_2$ oxidation protective coatings prepared by slurry painting for C/C-SiC composites, Surf. Coating. Technol. 202 (2008) 4734–4740.
[22] Y.L. Zhang, H.J. Li, Q.G. Fu, et al., A Si-Mo oxidation protective coating for C/SiC coated carbon/carbon composites, Carbon 45 (2007) 1130–1133.
[23] Chr Argirusis, T. Damjanovic, G. Borchardt, Yttrium silicate coating system for oxidation protection of C/C-Si-SiC composites: electrophoretic deposition and oxygen self-diffusion measurements, J. Am. Ceram. Soc. 27 (2007) 1303–1306.
[24] Yuanhao Li, Zhaofeng Chen, et al., Mechanical properties and failure mechanism of 3D needle-punched C$_f$/SiC-Al composites, Ceram. Int. 47 (2021) 33509–33514.
[25] L. Rangaraj, C. Divakar, V. Jayaram, Fabrication and mechanisms of densification of ZrB2-based ultra high temperature ceramics by reactive hot pressing, J. Eur. Ceram. Soc. 30 (1) (2010) 129–138.
[26] A M S, B D R B, Reactive melt infiltration of silicon-molybdenum alloys into microporous carbon preforms, Mater. Sci. Eng. 194 (1995) 193–200.
[27] H. Hatta, T. Takei, M. Taya, Effects of dispersed microvoids on thermal expansion behavior of composite materials, Mater. Sci. Eng. 285 (1–2) (2000) 99–110.
[28] C.R. Wang, J.M. Yang, W. Hoffman, Thermal stability of refractory carbide/boride composites, Mater. Chem. Phys. 74 (2002) 272–281.
[29] H. Dong, Z. Fa Ng, T. Yang, et al., Single crystalline 3C-SiC whiskers used for electrochemical detection of nitrite under neutral condition, Ionics 22 (2016) 1493–1500.
[30] W. Liu, J. Chen, T. Yang, et al., Enhanced photoluminescence properties of SiC/SiO$_2$ coaxial nanocables by making oxygen vacancies, Dalton Trans. 45 (34) (2016) 3503–13508.